LAWRENCE
LIVERMORE
NATIONAL
LABORATORY

LLNL-PROC-430616

ASPH modeling of Material Damage and Failure

J. M. Owen

May 6, 2010

5th International SPHERIC SPH Workshop
Manchester, United Kingdom
June 23, 2010 through June 25, 2010

Disclaimer

ASPH modeling of Material Damage and Failure

J. Michael Owen
Lawrence Livermore National Laboratory
M/S L-038
P.O. Box 808
Livermore, CA, USA
email: mikeowen@llnl.gov

***Abstract*—We describe our new methodology for Adaptive Smoothed Particle Hydrodynamics (ASPH) and its application to problems in modeling material failure. We find that ASPH is often crucial for properly modeling such experiments, since in most cases the strain placed on materials is non-isotropic (such as a stretching rod), and without the directional adaptability of ASPH numerical failure due to SPH nodes losing contact in the straining direction can compete with or exceed the physical process of failure.**

I. Introduction.

Modeling the processes of damage and fracture of materials is an area where meshless methods offer clear benefits over traditional mesh based hydrodynamic approaches. Damage models ([1], [6]) involve following history variables (such as a damage fraction) tied to distinct chunks of mass through large distortions in the fluid flow. These highly dynamic systems usually force mesh based methods to perform some sort of remap of the system in order to maintain a valid mesh, introducing diffusive errors into the history variables. Robust Lagrangian methods such as SPH solve this problem trivially as their Lagrangian nature is ideally suited for following properties tied to the mass distribution, though of course meshless methods come with their own difficulties.

One challenge modeling material fracture presents for a standard SPH approach is that the material strain field is often strongly anisotropic, implying that the nodes representing the material will undergo very anisotropic displacements. Consider a rod being pulled apart along its length: the nodes along the length of the rod will be separating, while the nodes across the width of the rod will actually be approaching one another as the rod compresses in that direction. This presents a problem for adapting the scalar smoothing scale h_i in SPH. The goal of adapting h_i is to keep the number of neighbors for each SPH node roughly constant, which in our tensile rod example will result in a compromise such that we preferentially sample more and more nodes across the width of the rod while simultaneously losing neighbors in the direction of stretching. The worst case scenario as this process continues is that the nodes will ultimately have too few neighbors in the stretching direction in numerical fracture will occur simply due to the nodes becoming decoupled.

One natural solution to this difficulty is to employ Adaptive Smoothed Particle Hydrodynamics (ASPH) [7], which replaces the scalar smoothing scale h_i of SPH with a symmetric tensor $H_i^{\alpha\beta}$. The use of $H_i^{\alpha\beta}$ allows the local sampling volume for each node to be an arbitrary ellipse in 2D/ellipsoid in 3D, freeing the technique from the unit aspect ratio sampling of SPH. The ASPH algorithm strives not just to keep a constant number of neighbors per node but also a constant number of neighbors *in each direction* around each node, ensuring problems such as numerical fracture in our tensile rod do not occur. In Fig. 1 we compare two different models of a 2D rod stretching horizontally, one SPH and one ASPH. The color scale is the magnitude of the damage being evolved on each node. The SPH model in Fig. 1(a) has failed numerically, evidenced by the fact that at the break points the damage variable does not indicate failure. By contrast the ASPH model in Fig. 1(b) has failed where the physical damage model indicates that it should. Fig. 2 compares the evolution of the sampling volume shapes in these two models. The SPH model in Fig. 2(a) shows the spherical sampling around each node overlapping extensively across the width of the rod while separating along the length, whereas the ASPH shapes in Fig. 2(b) demonstrate the successful adaptation of ASPH sampling volumes to distortion of the material.

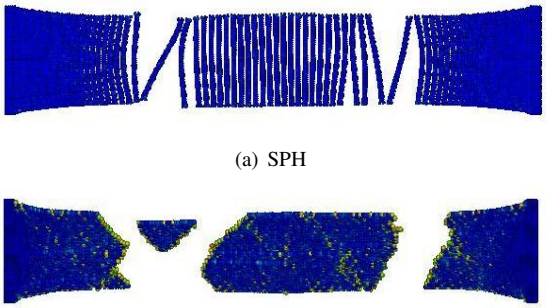

(a) SPH

(b) ASPH

Fig. 1. Damage magnitude for (a) SPH and (b) ASPH models of a stretching rod in 2D.

II. Choosing the SPH and ASPH smoothing transformations.

The ASPH fluid evolution equations are identical to the SPH forms if one appropriately removes the references to the smoothing scale by working in "normalized" coordinates η^α, where η^α is defined as $\eta^\alpha = x^\alpha/h_i$ in SPH and $\eta^\alpha = H_i^{\alpha\beta}x^\beta$ in ASPH. Note that $H_i^{\alpha\beta}$ has units of inverse length, and ASPH

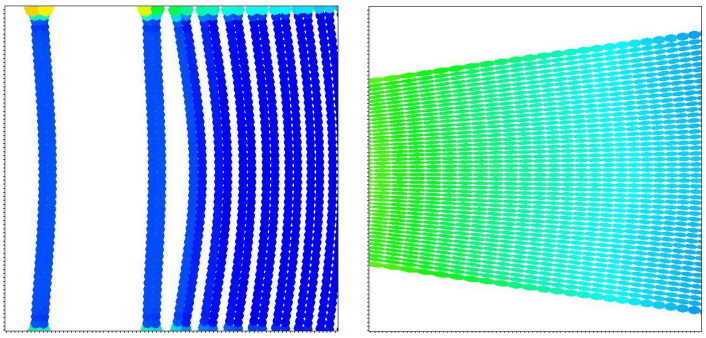

(a) SPH (b) ASPH

Fig. 2. A zoom in on the shapes of the local nodal sampling volume (essentially smoothing scale isocontours) for (a) SPH and (b) ASPH models of the stretching rod show in Fig. 1 before the onset of physical failure.

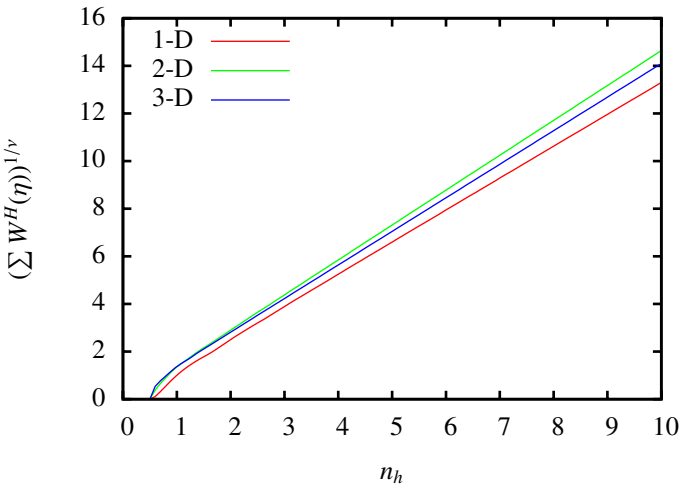

Fig. 3. Examples of the relation between $\Psi_0 = (\sum W^H(\eta))^{1/\nu}$ and the effective sampling size n_h for 1D, 2D, and 3-D kernels.

reduces to SPH in the limit of forcing $H_i^{\alpha\beta} = \delta^{\alpha\beta} h_i^{-1}$. In this section we will focus on the problem of how to choose an optimal h_i (SPH) or $H_i^{\alpha\beta}$ (ASPH) for each node.

In [7] we derive a time evolution equation for $DH_i^{\alpha\beta}/Dt$ based on the assumption that the local $H_i^{\alpha\beta}$ should try and track the local deformation of the fluid with time – this is equivalent to striving to keep the same set of neighbors for each node for all time. Note that some meshless approaches carry this approach to the extreme in keeping the set of neighbors constant for each point, sometimes referred to as the Lagrangian kernel. This approach works well for relatively simple velocity fields, but as the fluid flow becomes more complicated (particularly in the presence of vorticity) this approximation must break down. One simple example of such a system is a shear flow. If we try to employ our concept of following the same set of neighbors in a purely shearing flow then the sampling volumes represented by the ellipsoidal $H_i^{\alpha\beta}$ tensor will stretch and distort to arbitrarily extreme aspect ratios with time, despite the fact that the local nodal density is not changing. In fact the normal SPH answer of a spherical sampling volume is a fine solution to this system since the nodal density remains unchanged in all directions in a pure shear. Previously with just the Lagrangian definition of $DH_i^{\alpha\beta}/Dt$ we beat down such problems by simply periodically smoothing the $H_i^{\alpha\beta}$ field. This smoothing helps prevent the growth of noise in the $H_i^{\alpha\beta}$ field as well as tamp down unwanted evolution due to vorticity, but it also degrades much of our advantage in using ASPH since the smoothing leads to overly round $H_i^{\alpha\beta}$ tensors. A better solution is to develop an algorithm to choose appropriate $H_i^{\alpha\beta}$ tensors for any instantaneous distribution of nodes, rather than time evolving from a previous state. The goal of this "ideal H" algorithm is choose the $H_i^{\alpha\beta}$ field such that each node sees a roughly constant number of neighbors in each direction. Another way to express this algorithm is that if we view $H_i^{\alpha\beta}$ as a transformation into the normalized coordinate frame of η^α, then in the local η space the neighbors of node i should appear isotropic.

We will break up the task of finding the ideal $H_i^{\alpha\beta}$ into two pieces: finding the scalar sampling volume represented by the determinant $\|H_i^{\alpha\beta}\|$ discussed in §II-A, and finding the shape $\tilde{H}_i^{\alpha\beta}$ (where $\|\tilde{H}_i^{\alpha\beta}\| = 1$) in §II-B. These two elements then combine to give us the new $H_i^{\alpha\beta^{\text{new}}} = (\|H_i^{\alpha\beta}\|)^{1/\nu} \tilde{H}_i^{\alpha\beta}$.

A. *Choosing* $\|H_i^{\alpha\beta}\|$.

Determining the optimal sampling volume for $H_i^{\alpha\beta}$ is equivalent to finding an appropriate SPH smoothing scale h_i. We choose to express this as function of the effective number of nodes per smoothing scale, denoted by n_h. For a given sampling kernel W it is possible to build up a table of the expected $\sum W^H(\eta)$ as a function n_h by simply performing such a sum over a uniform lattice of points with the required spacing in η space. Fig. 3 shows one such parameterization for a kernel based on the popular cubic B spline kernel. We make the distinction of W^H vs. W here for reasons that are expanded on in §II-C – for our discussion now we can consider $W = W^H$. Note that in Fig. 3 we are actually plotting a root of the zeroth moment

$$\Psi_0 \equiv \left(\sum_j W^H(\eta_j) \right)^{1/\nu} \tag{1}$$

where ν is the dimensionality of the system (1D, 2D, or 3D) and $\eta_j = H_i^{\alpha\beta} x_{ij}^\beta$. This results in a nice linear relationship between Ψ_0 and n_h, which lends itself to interpolating for the effective n_h for any measured Ψ_0.

Once we have identified the effective n_h for a given node, it is simple to find the ratio $s \equiv n_h^{\text{target}}/n_h$, telling us how much we need to scale $\|H_i^{\alpha\beta}\|$ (or equivalently the SPH h_i) in order to get to our target number of nodes per smoothing scale n_h^{target}. In order to avoid instabilities with abruptly jumping around in $\|H_i^{\alpha\beta}\|$ we adopt an approach similar to that described in [9] and define

$$a = \begin{cases} s < 1 & : \quad 0.4(1 + s^2) \\ s \geq 1 & : \quad 0.4(1 + s^{-3}) \end{cases}, \tag{2}$$

$$h_i^{\text{new}} = (1 - a + as)h_i, \tag{3}$$

or equivalently for $\|H_i^{\alpha\beta}\|$

$$\|H_i^{\alpha\beta}\|^{\text{new}} = (1 - a + as)^{-\nu}\|H_i^{\alpha\beta}\|. \tag{4}$$

This whole procedure is very inexpensive – at simulation startup we tabulate the table of $\Psi_o(n_h)$ for the chosen kernel for a relevant range of n_h, from which we can make a rapid table lookup to get the effective n_h as a function of the current Ψ_0 for any node. Once we have the n_h we can immediately derive the new h_i for SPH (or $\|H_i^{\alpha\beta}\|$ for ASPH) according to Eqs. 2–4. We use this procedure to update h_i in all our SPH simulations, giving us reliable control of the effective n_h used. This algorithm converges at second-order for h_i, as we will expand upon in future publications.

B. Choosing the shape $\tilde{H}_i^{\alpha\beta}$.

In Appendix B of [7] we point out that the shape of the $H_i^{\alpha\beta}$ tensor can be related to the second moment of the point distribution about any given node i. We exploit this relationship here to derive the optimal shape for the new sampling volume $\tilde{H}_i^{\alpha\beta}$. We define the second moment of the local sampling weight as

$$\Psi_2^{\alpha\beta} = \sum_j \left(\frac{W^H(\eta_{ij})}{\eta_{ij}^{\nu-1}} \right)^2 \hat{x}_{ij}^{\alpha} \hat{x}_{ij}^{\beta}, \tag{5}$$

where $x_{ij}^{\alpha} = x_i^{\alpha} - x_j^{\alpha}$, $\eta_{ij} = H_i^{\alpha\beta} x_{ij}^{\alpha}$, and $\hat{x}_{ij}^{\alpha}$ is the unit vector in the direction of x_{ij}^{α}. We can relate the target shape for $\tilde{H}_i^{\alpha\beta}$ to the square root of the inverse of $\Psi_2^{\alpha\beta}$,

$$\tilde{H}_i^{\alpha\beta} = (\|\Psi_2^{\alpha\beta}\|)^{1/4} \left((\Psi_2^{-1})^{\alpha\beta} \right)^{1/2}. \tag{6}$$

We have deliberately made $\Psi_2^{\alpha\beta}$ a second moment of the local kernel weight because it is the weighting with distance that makes this sum sensitive to the local nodal spacing. One can easily see the problem with using a direct second moment of the node distribution: consider for instance a uniform node distribution which has been compressed in one direction. The distribution is still uniform in a volumetric sense (there is a constant density of nodes), so the second moment of the positions will be some scalar multiple of the unit tensor. However, this is precisely the type of situation in which we want the $H_i^{\alpha\beta}$ tensor to adapt to the compression in one dimension. The kernel weighting sensitivity of Eq. 5 builds in this sensitivity to spacing and results in the desired behaviour.

C. Choosing W^H.

In the relations for the zeroth and second moments Ψ_0 and $\Psi_2^{\alpha\beta}$ (Eqs. 1 and 5) we have made the distinction of the kernel used: W^H vs. W. The reason for this is due to the sets of nodes we wish to focus on. Typical interpolation kernels used for (A)SPH calculations are centrally peaked, such as the cubic B spline or Gaussian. There are good reasons this is desirable when evaluating gradients and derivatives, but we have found in practice centrally peaked kernels make the $H_i^{\alpha\beta}$ shape fitting too sensitive to the details of the nearest neighbor node. This problem is exacerbated in the presence of the well known tensile instability. Instead we have been much more successful choosing a kernel that is peaked at some intermediate distance from the central position, falling to zero at the both the center of the kernel and its extreme range. One simple choice for W^H that meets this goal is the magnitude of the gradient of the normal kernel: $W^H(\eta) = \|\partial_\eta W(\eta)\|$. Fig. 4 plots an example of what this looks like for the cubic B spline. You can see this form of W^H emphasizes the contributions of nodes at intermediate distances in the sampling volume, strongly deemphasizing contributions from very near neighbors. Experience has shown this effectively minimizes the effects of problems such as the tensile instability in ASPH calculations.

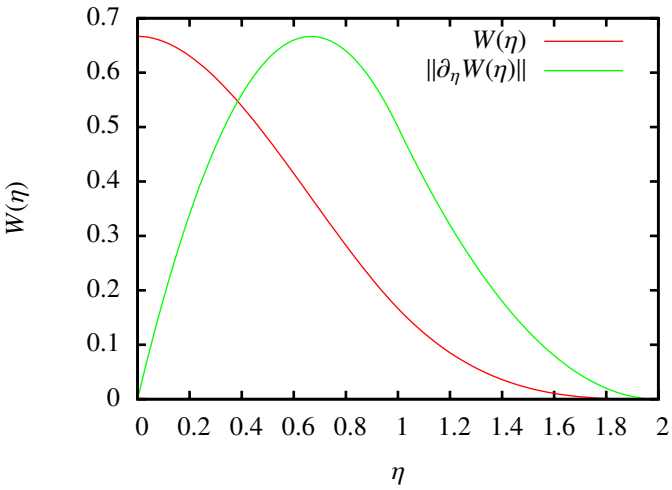

Fig. 4. Comparison of $W(\eta)$ and $W^H(\eta) = \|\partial_\eta W(\eta)\|$ for the cubic B spline kernel.

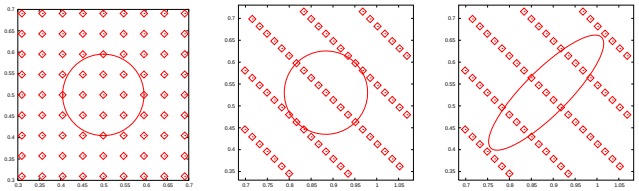

(a) Initial conditions (b) SPH (c) ASPH

Fig. 5. (a) Initial nodal positions and the associated $\eta = 1$ isocontour of $H_i^{\alpha\beta}$. Panels (b) and (c) show the SPH and ASPH (respectively) fitted results for a volume preserving distortion of the node positions.

D. An idealized example.

The combination of Eqs. 1, 4, 5, & 6 provide us with a low cost method of defining the the new $\tilde{H}_i^{\alpha\beta}$ field for any nodal distribution. The necessary sums of W^H can be performed at the same time we are evaluating the ASPH dynamical equations, so the overhead is minimal. In Fig. 5 we show an example applying these algorithms to find the new SPH and ASPH sampling volumes for a node distribution which is

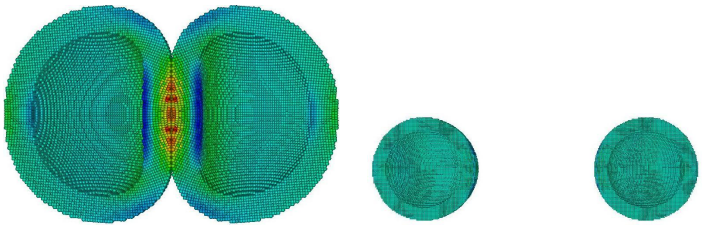

(a) Maximum compression (b) Post-bounce

Fig. 6. The colliding rubber balls test of the tensile instability, colored by pressure. Panel (a) represents the maximum deformation at the peak of the collision, while panel (b) is long after the balls have bounced and are separating.

distorted in a volume preserving manner – the initial nodes in Fig. 5(a) are rotated by 45°, stretched by a factor of 2 along one axis of the lattice, and compressed by a factor of 2 in the other. Since this distortion is volume preserving the SPH solution remains unchanged, while the ASPH solution adjusts to the rotation, compression, and expansion as expected.

E. The choice of n_h^{target}.

Before we proceed to the comparison of simulations with complicated experimental setups we should mention the subject of choosing the target number of nodes per smoothing scale n_h^{target}. It is well known that the accuracy of SPH simulations can be a function of n_h^{target}, and we have found that it is critical to use adequate sampling (a large enough value of n_h^{target}) in order to get good results for the shape $\tilde{H}_i^{\alpha\beta}$. Experimentally we have found the $n_h^{\text{target}} \sim 2$ works quite well, which is roughly 1.5–2 times the typical choice for this parameter. However, for values significantly below 2 we find that both SPH and ASPH results degrade significantly – with too few neighbors the noise/discreteness effects due to poor representation of the numerical gradients can be raised to the point that the order of convergence or even stability of the system suffers. One effect we have noticed by increasing $n_h^{\text{target}} \sim 2$ is that the tensile instability of SPH is significantly reduced. As an example of this improvement we present the results of running a well known test of the tensile instability in Fig. 6: the collision of two rubber balls (see description in [5]). When run with the usual choice of $n_h^{\text{target}} \leq 1.2$ we see failure of this problem to survive a single bounce as described in [5]. However, as is evident in Fig. 6(a) with $n_h^{\text{target}} = 2$ even at maximum compression the balls show no sign of instability. We follow the evolution of the system through many post-bounce oscillations to significantly later times (shown in Fig. 6(b)) with no sign of instability. Note this is all done without using any sort of fix-up for the tensile instability such as described in [5]. We therefore recommend that ASPH simulations be run with $n_h^{\text{target}} \in [1.5, 2]$ at all times, preferring the larger value of 2. The penalty of course is the significant increase in number of neighbors and therefore computational expense as compared with more typical values of $n_h^{\text{target}} \in [1, 1.2]$.

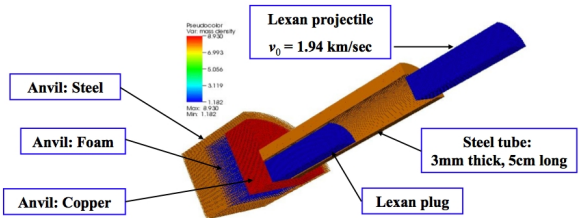

Fig. 7. Initial conditions (mass density) for the gas gun driven rupture of a steel tube.

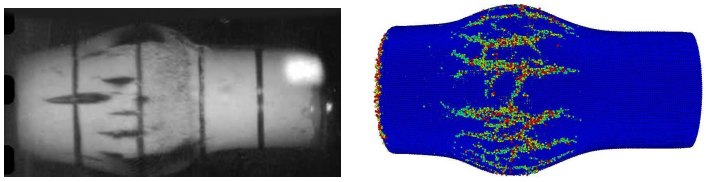

(a) Experiment (b) Simulation

Fig. 8. (a) Experimental photograph and (b) damage magnitude from simulation of the rupturing steel tube gas gun experiment early in the process of failure.

III. Examples.

In this section we will present several results applying the ASPH formalism to problems of material fracture and failure. Due to the space constraints we will not delve into all the details of our equations here, but rather we refer the reader to [7] for the general ASPH fluid equations, [5] for the solid mechanics forms of these equations, and [1] for information on damage modeling. We note parenthetically we have extended the damage model in particular: we employ a tensor damage variable for each node which evolves the damage independently along each axis of the tensor according to a tensor measure of the material strain. This tensor strain is a history variable determined by the local differential velocity field – it is not aligned with any particular coordinate system and the eigen vectors of the strain and damage evolve and change orientation appropriately due to the material deformation. We also employ a modification of the usual energy equations that exactly conserves the total energy. Our methodology for the specific thermal energy update is based upon the ideas in [3], and is explained in detail in a preprint available at [8].

A. Gas gun driven rupture of a steel tube.

Our first example problem is an experiment described in [10] wherein a plastic projectile is fired by a gas gun into hollow steel tube half-filled with a plastic plug. The projectile impacts the plug and expands against the tube internally, causing it to rupture. Fig. 7 shows a cutaway view of the initial conditions for this problem. In Fig. 8 we compare a photograph from the experiment early on as the tube is rupturing with an image from the simulation at the same stage. We can see qualitatively the rupturing in the simulation is similar to the experiment, with the ruptures first occurring along the length of the tube. Fig. 9 shows an end on view of the fragmentation process in the simulation at much later time.

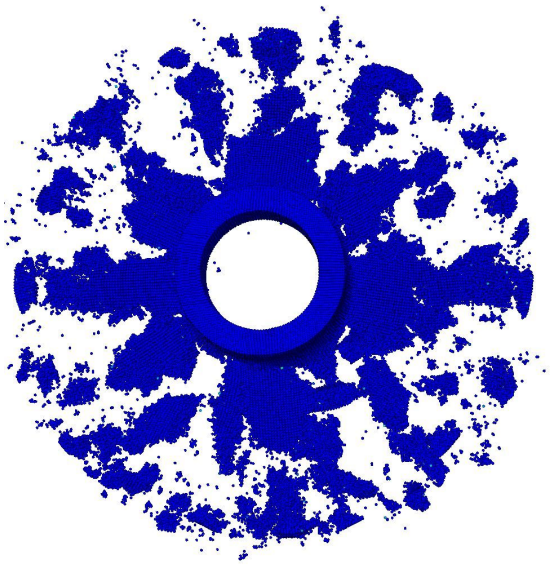

Fig. 9. An end on view of the gas gun experiment at late time, demonstrating the fragmentation process as the pieces begin to separate.

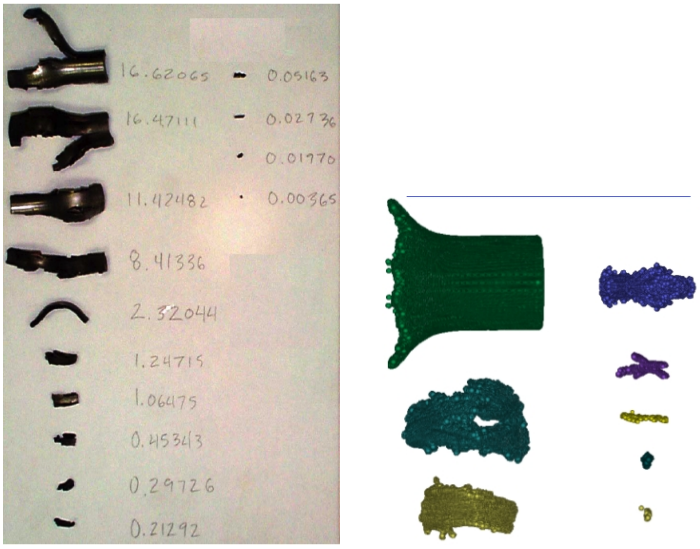

(a) Recovered Fragments (b) Simulated Fragments

Fig. 11. Comparison of the experimentally recovered fragments from the gas gun experiment with fragments identified in the simulation.

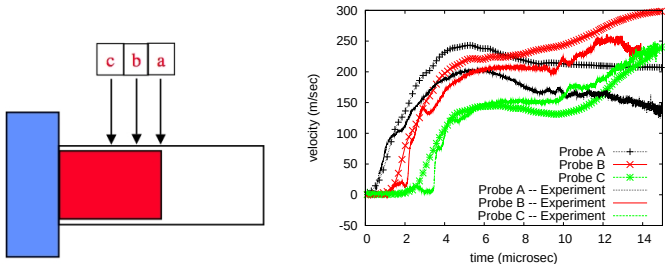

(a) VISAR probes (b) VISAR traces

Fig. 10. (a) Diagram of the placement of the VISAR velocimetry probes along the tube for the gas gun experiment, and (b) comparison of experiment and simulation for these diagnostics.

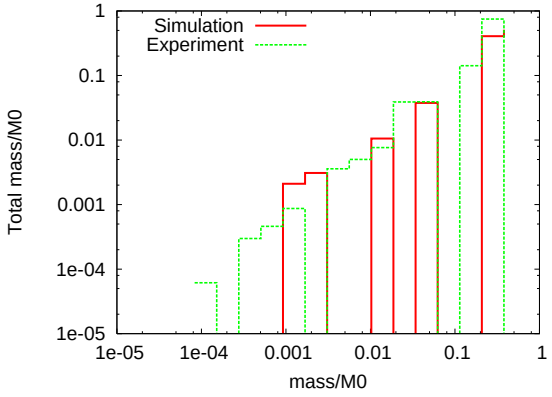

Fig. 12. Histogram of the total mass in fragments in bins of individual fragment masses.

We prefer more quantitative comparisons of the simulation and experiment, so in Fig. 10(b) we examine results for three different VISAR velocimetry probes of the expansion of the tube at different points along its length: probe A is 2.5cm from the anvil, probe B 2cm, and probe C 1.5cm. This is a fairly sensitive test, and we can see that while the simulation reproduces the qualitative behaviour of the measurements, probes A and B show too much velocity relative to the experimental diagnostics. Clearly there is room for improvement here.

Another diagnostic of interest is the distribution of fragments. This experiment uses soft-capture to recover much of the mass of the tube, which we can compare with the population of simulated fragments identified by a friends of friends algorithm once the simulation progresses such that the fragments are well separated. In Fig. 11 we show a comparison of of the morphology of the experimental and simulated fragment populations. Fig. 12 plots a histogram of the total mass in fragments as a function of the fragment mass for both the recovered and simulated fragments. The results seem in reasonable agreement, though of course we are dealing with a small number population of fragments.

B. HE driven fragmentation of a steel spherical section.

Another interesting fragmentation experiment is described in [2]. This experiment is a high explosive driven expansion of a section of a steel spherical shell. Fig. 13 shows a cutaway of the initial conditions for this experiment. The detonator is placed in the center rear of this geometry, which will result in a detonation wave that sweeps out over the steel shell, straining and ultimately fragmenting it as it expands away from the high explosive. Fig. 14 compares a series of snapshots from the experiment alongside images of the damage variable in the simulation at the same times. We can clearly see the characteristic flaking pattern of the fragmentation forming in the simulation. The surface of the steel in the experimental photos shows evidence of this fragmentation in striations we

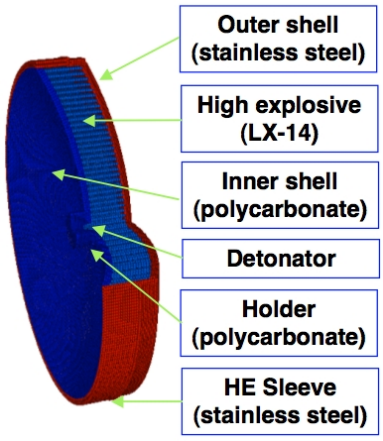

Fig. 13. Cutaway view of the initial geometry for the high explosive driven spherical steel section.

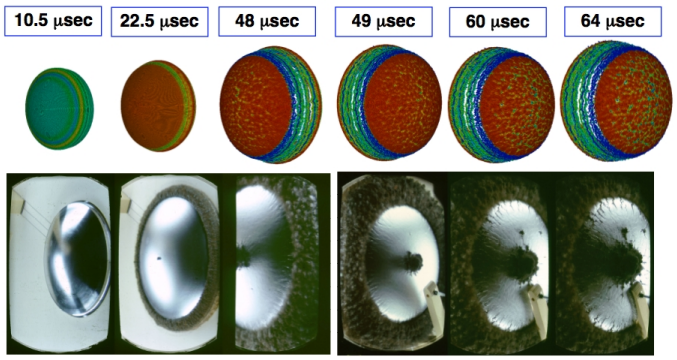

Fig. 14. Time sequence of the expansion and fragmentation of the high explosive driven steel spherical shell. The lower images are snapshots from high speed photographs of the experiment, while the upper panels are images of the damage in the simulation at the same times.

can see spreading over the surface of the steel as well as the escape of the detonation products in the expanding cloud appearing around the edges.

This experiment also featured a velocimetry probe. The probe can be seen in the photographs in Fig. 14 – it is the tan colored arm seen projecting in from the side. Fig. 15 plots the experimental velocimetry trace vs. several different points at the same radius in the simulation. In this case we clearly match the experimental velocimetry better than in the expanding tube, though the pull back seen in the velocity during the rise of the experimental curve is not as distinct in the simulated version. We also have fragment population data from this experiment as well, though the recovered mass in fragments only amounts to 60% of the mass of the shell (excluding the steel ring). Fig.16 compares the simulated fragment population to the experimentally recovered set. Since the experiment did not recover all fragments we plot these distribution here as fractional distributions of the total. It appears we match the fragment distributions quite well for this experiment.

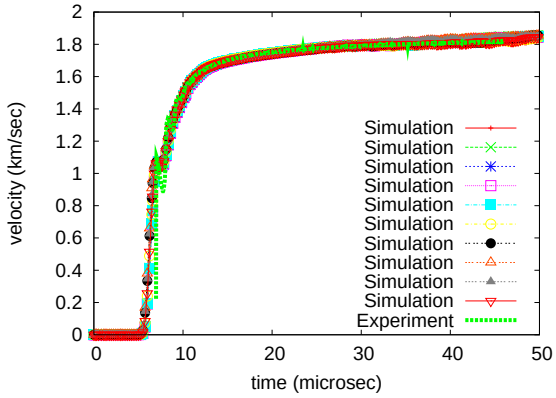

Fig. 15. Velocimetry comparison for the expanding steel spherical shell.

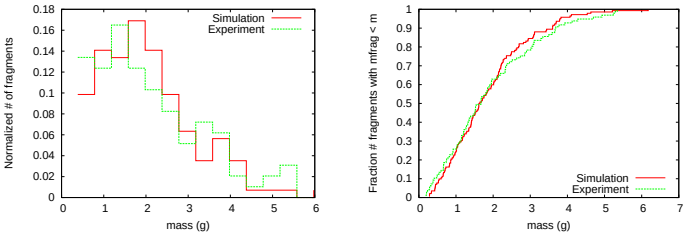

(a) Binned fragment distribution (b) Cumulative fragment distribution

Fig. 16. Fragment distribution properties for the steel spherical shell 2 experiment.

C. HE driven fragmentation of a steel tube.

Our final example is something of a combination of the previous two: the high explosive driven fragmentation of a steel cylinder. This experiment is described in [4]; the initial geometry for our model is shown in Fig. 17. This experiment is lighted on the LX-10 booster at the top, and as the detonation wave proceeds down the high explosive it expands and fragments the tube. In Fig.18(a) we see the detonation wave in the pressure proceeding down the cylinder as the high

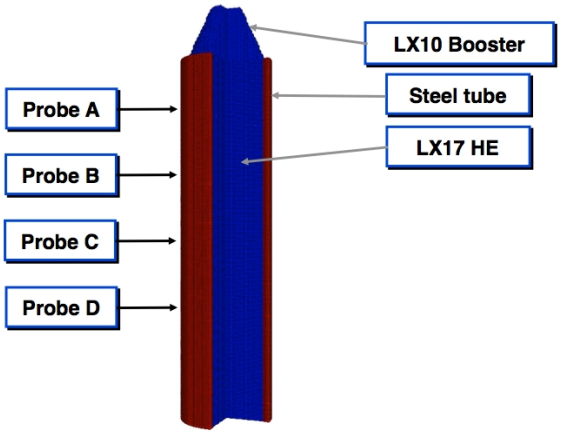

Fig. 17. Cutaway view of initial geometry for the high explosive driven steel tube experiment.

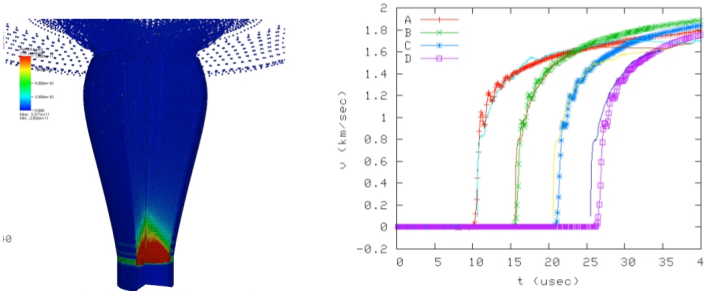

(a) Pressure (b) Velocimetry

Fig. 18. The (a) pressure at 50 μsec and (b) velocimetry for the high explosive steel tube.

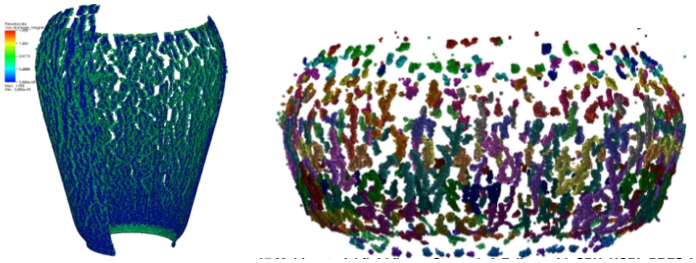

(a) Damage (b) Simulated Fragments

Fig. 19. (a) Damage in the tube at 50μsec leading to fragmentation. (b) Simulated steel colored by fragment identification at 150μsec.

explosive burns. Note the evident pressure waves in the steel following the detonation front – these waves contribute to the strain history and therefore damage to the cylindrical shell. Fig. 18(b) compares the velocimetry from the experiment with the simulation at four points along the length of the cylinder. In this simulation we have put adequate resolution through the thickness of the tube so that we have captured the pull back signal more effectively than in the previous examples.

Examination of the simulated fragments as they form in Fig. 19 shows that we are generating long thin fragments roughly aligned with the length of the tube. This makes physical sense since initially the dominant strain mechanism is a hoop strain going around the circumference of the tube

Fig. 20. Examples of the experimentally recovered fragments from the high explosive tube.

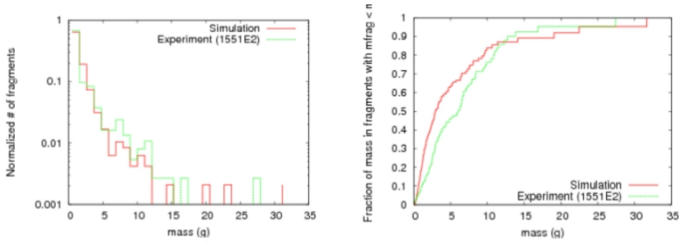

(a) Binned Fragment Distribution (b) Cumulative Fragment Mass Distribution

Fig. 21. Fragment population distributions for the high explosive steel tube experiment. Panel (a) shows the numbers of fragments binned as a function of fragment mass, while panel (b) plots the cumulative mass in fragments as a function of fragment mass.

which would tend to form fragments as strips, which then break into smaller pieces as the fracture planes randomly cross. This seems to match the qualitative morphology of the experimentally recovered fragments in Fig. 20.

In Fig. 21 we compare the fragment mass distributions between the ASPH simulation and experiment. The simulated and experimental distributions are close, but there seems to be a trend for the simulation to overproduce low mass fragments compared with the simulation. This effect is not large, and there are several potential causes to consider. It is possible that this effect may be due to a biasing effect with the soft recovery from the experiment that preferentially loses low mass fragments, which would be very difficult to test. It is also possible that the simulated fragments tend to have a lower mass due to the loss of fully damaged ASPH nodes (essentially an erosion due to how we damage the material). If true, we would expect this effect should diminish with increasing simulation resolution, and perhaps the simulation would converge upon the experimental result. It's also possible we simply do not have the damage parameters quite correct for steel. These various explanations remain to be tested.

IV. Conclusion.

We have discussed some our latest improvements in the ASPH methodology, in this case highlighting new algorithms for determining the $H_i^{\alpha\beta}$ smoothing scale tensor from first principles for any distribution of ASPH nodes. This represents a significant improvement over our original methodology published in [7]: we remove the necessity for periodic smoothing of the $H_i^{\alpha\beta}$ field as well as make the the choice of $H_i^{\alpha\beta}$ robust in arbitrarily complex fluid flows. We find that the flexibility of ASPH in fitting arbitrarily anisotropic nodal distributions in important for modeling the failure and fragmentation of materials due to the generally anisotropic nature of the material distortion. Without the adaptability of ASPH it possible for numerical fracture to occur and preempt the physically motivated fragmentation of materials. The ability to use non-unit aspect ratio sampling also assists in setting up models of materials consisting of large thin shells of material, a situation we see in the examples presented in §III-B and §III-C.

While the results comparing our ASPH simulations to experimental results in §III generally work well, there is much room for improvement. In particular we would like to explore using the tensor smoothing scale methodology described here with the improved discretization numerics of one of the forms of Corrected SPH (CSPH). The hope is that such numerical improvements will lead to better fits for diagnostics such as the velocimetry traces from these experiments, and overall more accuracy in the models.

ACKNOWLEDGMENT.

This work was performed under the auspices of the U.S. Department of Energy by Lawrence Livermore National Laboratory in part under Contract W-7405-Eng-48 and in part under Contract DE-AC52-07NA27344.

REFERENCES

[1] W. Benz and E. Asphaug, Computer Physics Communications, 87, 253-265, 1995.
[2] G. H. Campbell, G. C. Archbold, O. A. Hurricane, and P. L. Miller, Journal of Applied Physics, 101, 033540, 2007.
[3] E. J. Caramana, D. E. Burton, M. J. Shashkov, and P. P. Whalen, J. Comp. Phys., 146, 227-262, 1998.
[4] D. M. Goto, R. Becker, T. J. Orzechowski, H. K. Springer, A.J. Sunwoo, and C. K. Syn, Int. J. Impact Engn, 35, 1547-1556, 2008.
[5] J. P. Gray, J. J. Monaghan, and R. P. Swift, Comput. Methods Appl. Mech. Engrg., 190, 6641-6662, 2001.
[6] G. R. Johnson and W. H. Cook, Engineering Fracture Mechanics, 21, No. 1, 31-48, 1985.
[7] J. M. Owen, J. V. Villumsen, P. R. Shapiro, and H. Martel, Astrophys. J. Supp., 116, 155-209, 1998.
[8] J. M. Owen, preprint, available at http://arxiv.org/abs/0906.3029v1.
[9] R. J. Thacker, E. R. Tittley, F. R. Pearce, H. M. P. Couchman, and P. A. Pearce, MNRAS, 319, 619, 2000.
[10] T. J. Vogler, T. F. Thornhill, W. D. Reinhart, L. C. Chhabildas, D. E. Grady, L. T. Wilson, O. .A. Hurricane, and A. Sunwoo, Int. J. Impact Engng, 29, 735-746, 2003.